Coulomb interaction, phonons, and superconductivity in twisted bilayer graphene

Tommaso Cea[a,b] and Francisco Guinea[a,c,d,1]

[a]IMDEA Nanoscience, 28015 Madrid, Spain; [b]Instituto de Ciencia de Materiales de Madrid, Consejo Superior de Investigaciones Científicas, 28049 Madrid, Spain; [c]Donostia International Physics Center, 20018 San Sebastián, Spain; and [d]Ikerbasque Basque Foundation for Science, 48009 Bilbao, Spain

Contributed by Francisco Guinea, June 8, 2021 (sent for review April 26, 2021; reviewed by Liang Fu and Yuval Oreg)

The polarizability of twisted bilayer graphene, due to the combined effect of electron–hole pairs, plasmons, and acoustic phonons, is analyzed. The screened Coulomb interaction allows for the formation of Cooper pairs and superconductivity in a significant range of twist angles and fillings. The tendency toward superconductivity is enhanced by the coupling between longitudinal phonons and electron–hole pairs. Scattering processes involving large momentum transfers, Umklapp processes, play a crucial role in the formation of Cooper pairs. The magnitude of the superconducting gap changes among the different pockets of the Fermi surface.

graphene | superconductivity | twisted

Twisted bilayer graphene (TBG) shows a complex phase diagram which combines superconducting and insulating phases (1, 2) and resembles strongly correlated materials previously encountered in condensed matter physics (3–6). On the other hand, superconductivity seems more prevalent in TBG (7–11), while in other strongly correlated materials magnetic phases are dominant.

The pairing interaction responsible for superconductivity in TBG has been intensively studied. Among other possible pairing mechanisms, the effect of phonons (12–19) (see also ref. 20), the proximity of the chemical potential to a van Hove singularity in the density of states (DOS) (21–25) and excitations of insulating phases (26–28) (see also refs. 29–31), and the role of electronic screening (32–35) have been considered.

In the following, we analyze how the screened Coulomb interaction induces pairing in TBG. The calculation is based on the Kohn–Luttinger formalism (36) for the study of anisotropic superconductivity via repulsive interactions. The screening includes electron–hole pairs (37), plasmons (38), and phonons (note that acoustic phonons overlap with the electron–hole continuum in TBG). Our results show that the repulsive Coulomb interaction, screened by plasmons and electron–hole pairs only, leads to anisotropic superconductivity, although with critical temperatures of order $T_c \sim 10^{-3}$ to 10^{-2} K. The inclusion of phonons in the screening function substantially enhances the critical temperature, to $T_c \sim 1$ to 10 K.

The Model

Electronic Structure and Electron–Electron Interactions. The long-range Coulomb interaction, projected onto the central bands of TBG, is described by an energy scale in the range of 20 to 100 meV. As a result, this interaction modifies significantly the shape and width of the bands of TBG near the first magic angle. The Hartree potential widens the bands, as it shifts the energies at the K and M points of the moiré Brillouin zone (BZ) with respect to those at the Γ point (39–43). The inclusion of the exchange term in a full Hartree–Fock calculation leads to broken symmetry phases, with valley and/or spin polarization (44–47), among other possible phases (see also refs. 47–50).

In the following, we consider the role of long-range charge fluctuations in the superconducting pairing of TBG. These fluctuations couple to quasiparticles, and also among themselves, via the long-range Coulomb interactions. In addition, long-range fluctuations can be induced by longitudinal acoustic phonons (see below and also ref. 36), so we include these phonons in the calculation.

We analyze pairing by charge fluctuations using the leading contributions in perturbation theory, already considered in ref. 36. We describe, however, the charge fluctuations using the random phase approximation (RPA) response function, as the large DOS and the spin and valley multiplicities imply a significant renormalization of these excitations.

We analyze phases without broken symmetries, where pairing occurs between electrons in different valleys. This analysis can be extended to broken symmetry phases where the two valleys are partially occupied, as expected (45, 51) for fillings $\nu = \pm 2$.

We do not consider here pairing due to optical phonons, or to acoustic phonons which do not induce long-wavelength charge fluctuations. We discuss later whether these interactions enhance, or suppress, the pairing analyzed here.

The self-consistent screening of the long-range interactions, mediated by the long-wavelength charge excitations, is approximated by the static response function. The neglect of retardation effects, imposed by the complexity of the calculation, implies that pairing is overestimated when the obtained critical temperature is comparable to the frequencies where the response function is expected to have significant structure, such as the phonon frequencies.

The electronic properties of the model are described by the continuum model for TBG (52, 53), using the parameters in ref. 54, $\hbar v_F = 5.18$ eV Å, $\{g_{AA}, g_{AB}\} = \{0.0797\,\text{eV}, 0.0975\,\text{eV}\}$

Significance

We study the low-energy excitations in twisted bilayer graphene, including particle–hole excitations, plasmons, and acoustic phonons. We analyze the way in which these excitations lead to superconductivity, by means of well-tested diagrammatic techniques. We obtain critical temperatures of magnitude ∼1 to 10 K. We estimate the order parameter, which displays different values in different pockets of the Fermi surface. Umklapp processes due to large momentum exchange are crucial for the formation of superconductivity. We provide estimates and trends in agreement with the experimental measurements, emphasizing the tunability of superconductivity with the electronic band structure close to the Fermi level.

Author contributions: T.C. and F.G. designed research, performed research, analyzed data, and wrote the paper.

Reviewers: L.F., Massachusetts Institute of Technology; and Y.O., Weizmann Institute of Science.

The authors declare no competing interest.

[1]To whom correspondence may be addressed. Email: paco.guinea@imdea.org.

This article contains supporting information online at https://www.pnas.org/lookup/suppl/doi:10.1073/pnas.2107874118/-/DCSupplemental.

Published August 6, 2021.

(see *SI Appendix*, section 1 for further details). The difference between g_{AA} and g_{AB}, as described in ref. 54, accounts for the inhomogeneous interlayer distance, which is minimum in the AB/BA regions and maximum in the AA ones, or it can be seen as a model of a more complete treatment of lattice relaxation (55).

Electron–Phonon Interactions. We consider as well the electron–electron interaction mediated by acoustic phonons. The energy of these phonons, for wavelengths similar to the moiré unit cell, are of the order of 1 to 4 meV, comparable to the energy of electron–hole interactions. We focus on longitudinal phonons, which couple to electrons via the deformation potential, $D \sim 20$ eV. We neglect the interaction between phonons in the two layers and consider the even superposition of a phonon in each layer such that the displacements in the two layers have the same sign. We neglect the odd superposition, which induces shifts in the chemical potential of the two layers of opposite sign, so that it does not lead to a net charge accumulation. The exchange of a phonon leads to an effective, momentum and frequency dependent interaction between electrons:

$$\mathcal{V}^{ph}_{eff}(\vec{q},\omega) = \frac{D^2|\vec{q}|^2}{\rho(\omega^2-\omega^2_{\vec{q}})}, \qquad [1]$$

where ρ is the mass density, $\omega_{\vec{q}} = v_s|\vec{q}|$ is the frequency of a phonon of momentum $\vec{q}$, and $v_s = \sqrt{(\lambda+2\,\mu)/\rho}$ is the velocity of sound, λ and μ being the elastic Lamé coefficients. At low frequencies the electron–phonon coupling, in a single graphene layer, can be described by a dimensionless parameter which describes the phonon induced electron–electron interaction: $\tilde{g} = D^2/(\lambda+2\,\mu)\times|\chi_0|$, where χ_0 is the electronic susceptibility at zero frequency and momentum (see also ref. 56).

We use $\lambda+2\,\mu \approx 20$ eV Å^{-2} and $\chi_0 = -\mathcal{D}(\epsilon_F) \sim 4\times(WA_C)^{-1} \approx 2\times10^{-2}$ eV^{-1} Å^{-2}, where $\mathcal{D}(\epsilon_F)$ is the DOS at the Fermi energy, $W \sim 10$ meV is the electron bandwidth, $A_C \sim 2\times10^4$ Å^2 is the area of the unit cell, and the factor 4 stands for the spin and valley degeneracy. Then, the dimensionless electron–phonon interaction is $\tilde{g} \approx 0.4$. For a more detailed description of the phonons in TBG see *SI Appendix*, section 3.

Polarizability. Including the diagrams in Fig. 1, *Top*, the full polarizability of the system can be written as

$$\chi_{\vec{G},\vec{G}'}(\vec{q},\omega) = \sum_{\vec{G}''}\chi^0_{\vec{G},\vec{G}''}(\vec{q},\omega)\times\Big\{\delta_{\vec{G}'',\vec{G}'} - \Big[\mathcal{V}_C(\vec{q}+\vec{G}'') + \mathcal{V}^{ph}_{eff}(\vec{q}+\vec{G}'',\omega)\Big]\chi^0_{\vec{G}'',\vec{G}'}(\vec{q},\omega)\Big\}^{-1}_{\vec{G}'',\vec{G}'}, \qquad [2]$$

where $\chi^0_{\vec{G},\vec{G}''}(\vec{q},\omega)$ is the bare electronic polarizability (the bubble diagram in Fig. 1), $\mathcal{V}_C(\vec{q}) = 2\pi e^2\tanh(d_g|\vec{q}|)/(\epsilon|\vec{q}|)$ is the Coulomb potential, d_g is the distance of the sample from a metallic gate, ϵ is the screening from the external environment, and the vectors $\vec{G}$'s are reciprocal lattice vectors. We use $d_g = 40$ nm and $\epsilon = 10$. The susceptibility in Eq. **2** is a matrix with entries labeled by reciprocal lattice vectors.

The polarization in Eq. **2** allows us to define the screened Coulomb interaction:

$$\mathcal{V}^{scr}_{\vec{G},\vec{G}'}(\vec{q},\omega) = \epsilon^{-1}_{\vec{G},\vec{G}'}(\vec{q},\omega)\mathcal{V}_C(\vec{q}+\vec{G}'), \qquad [3]$$

with:

$$\epsilon_{\vec{G},\vec{G}'}(\vec{q},\omega) = \delta_{\vec{G},\vec{G}'} - \mathcal{V}_C(\vec{q}+\vec{G})\chi^{ph}_{\vec{G},\vec{G}'}(\vec{q},\omega), \qquad [4]$$

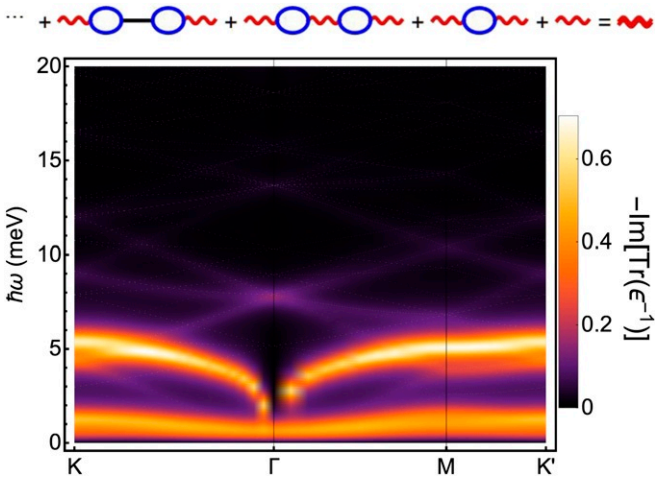

Fig. 1. (*Top*) Feynman diagrams included in the screened electron–electron interaction. Red wavy lines stand for the Coulomb interaction, and straight black lines stand for the electron–phonon interaction. (*Bottom*) Momentum and frequency dependence of the imaginary part of the inverse dielectric function, $-\mathrm{Im}\mathrm{Tr}\,\epsilon^{-1}_{\vec{G},\vec{G}'}(\vec{q},\omega)$; see Eq. **4**. The calculation is done at the magic angle, $\theta = 1.085°$, and at half filling. Due to the flatness of the bands, the system is metallic, and it has plasmons (*Results* and Fig. 2*B*).

where $\chi^{ph}_{\vec{G},\vec{G}'}(\vec{q},\omega)$is given by an expression similar to Eq. **2**, except that only the phonon interaction is included, in order to avoid double counting.

The diagrams which describe the screened interaction are shown in Fig. 1, *Top*. A plot of the imaginary part of the screening function, Eq. **4**, is shown in Fig. 1, *Bottom*. This figure measures the density of charge density excitations, weighted by their coupling to the electron quasiparticles. The lower horizontal bright bands show the electron–hole continuum, the bands directly above them are the plasmons (38), and the faint blue lines give the renormalized plasmons, broadened by their interaction with the electron–hole continuum.

The analysis includes Umklapp processes which enter both in the electron–electron and in the electron–phonon interaction. The calculation in Fig. 1 describes as well the plasmons of the system (38). Further results concerning the plasmon spectrum are reported in *SI Appendix*, section 2.

Superconducting Pairing via the Screened Coulomb Interaction. We consider pairing mediated by the screened interaction defined in Eq. **3**. This scheme is a variation of the method described in ref. 36. The polarization diagrams are iterated to infinity, using the RPA, while other, exchange-like, diagrams are not considered. The use of the RPA is justified as the spin and valley degeneracy enhances the contribution of diagrams with closed electron–hole bubbles over exchange-like diagrams.

The analysis of the pairing can be turned into a self-consistency condition for the propagator of a Cooper pair, or, alternatively, for the off-diagonal self-energy which hybridizes electrons and holes. This self-consistency requirement reduces to an eigenvalue problem near T_c, where the off-diagonal self-energy tends to zero. In real space and imaginary Matsubara frequencies, this linear equation is given by Eq. **5**:

$$\Delta^{i_1 i_2}_{\alpha\beta}(\vec{r}_1,\vec{r}_2) = -\sum_{i\omega'}\mathcal{V}^{scr}(\vec{r}_1,\vec{r}_2,i\omega-i\omega') \times\int_\Omega d^2\vec{r}_3 d^2\vec{r}_4\sum_{i_3 i_4}K_B\,T\mathcal{G}^{i_1 i_3}_{\vec{r}_1\vec{r}_3,\alpha}(i\omega') \times\mathcal{G}^{i_2 i_4}_{\vec{r}_2\vec{r}_4,\beta}(-i\omega')\Delta^{i_3 i_4}_{\alpha\beta}(\vec{r}_3,\vec{r}_4), \qquad [5]$$

where α, β label the spin/valley flavor, i_1, i_2, i_3, i_4 are sublattice and layer indices, Ω is the area of the system, and the $\mathcal{G}$ are the Green's functions, which can be written as

$$\mathcal{G}^{ij}_{\vec{r}\vec{r}',\alpha}(i\omega) = \sum_{n\vec{k}} \frac{\Phi^{i}_{n\vec{k},\alpha}(\vec{r})\Phi^{j,*}_{n\vec{k},\alpha}(\vec{r}')}{i\hbar\omega + \mu - E_{n\vec{k},\alpha}}, \quad [6]$$

where n labels the band and $\vec{k}$ the wave vector in the moiré BZ, $E_{n\vec{k},\alpha}$ is the band dispersion, μ is the chemical potential, and $\Phi_{n\vec{k},\alpha}$ is the Bloch's eigenfunction corresponding to the eigenvalue $E_{n\vec{k},\alpha}$:

$$\Phi^{i}_{n\vec{k},\alpha}(\vec{r}) = \frac{e^{i\vec{k}\cdot\vec{r}}}{\sqrt{\Omega}} \sum_{\vec{G}} \phi^{i}_{n\vec{k},\alpha}(\vec{G}) e^{i\vec{G}\cdot\vec{r}}, \quad [7]$$

where the ϕ's are eigenvectors amplitudes, normalized according to: $\sum_{\vec{G},i} \phi^{i,*}_{n\vec{k},\alpha}(\vec{G})\phi^{i}_{m\vec{k},\alpha}(\vec{G}) = \delta_{nm}$.

We can sum over the Matsubara frequencies analytically by considering the static limit of the screened potential in Eq. **5**: $\mathcal{V}^{scr}(\vec{r}_1, \vec{r}_2, i\omega - i\omega') \simeq \mathcal{V}^{scr}(\vec{r}_1, \vec{r}_2, i\omega = 0)$. Using this approximation (to be discussed further below) we obtain the following equation for the order parameter:

$$\tilde{\Delta}^{m_1 m_2}_{\alpha\beta}(\vec{k}) = \sum_{n_1 n_2} \sum_{\vec{q}} \Gamma^{m_1 m_2}_{n_1 n_2;\alpha\beta}(\vec{k}, \vec{q}) \tilde{\Delta}^{n_1 n_2}_{\alpha\beta}(\vec{q}), \quad [8]$$

where $\tilde{\Delta}^{m_1 m_2}_{\alpha\beta}(\vec{k})$ defines the amplitude for the pairing between the bands m_1 and m_2, and the kernel Γ is given by

$$\begin{aligned}
&\Gamma^{m_1 m_2}_{n_1 n_2;\alpha\beta}(\vec{k}, \vec{q}) = \\
&-\frac{1}{\Omega} \sum_{\vec{G}_1 \vec{G}_1'} \sum_{\vec{G}_2 \vec{G}_2'} \sum_{i_1 i_2} \mathcal{V}^{scr}_{\vec{G}_1 - \vec{G}_1', \vec{G}_2 - \vec{G}_2'} \left(\vec{k} - \vec{q}\right) \times \\
&\times \phi^{i_1,*}_{m_1 \vec{k},\alpha}(\vec{G}_1) \phi^{i_2,*}_{m_2 - \vec{k},\beta}\left(\vec{G}_2'\right) \phi^{i_1}_{n_1 \vec{q},\alpha}\left(\vec{G}_1'\right) \phi^{i_2}_{n_2 - \vec{q},\beta}(\vec{G}_2) \times \\
&\times \sqrt{\frac{f\left(-E_{m_2 - \vec{k},\beta} + \mu\right) - f\left(E_{m_1 \vec{k},\alpha} - \mu\right)}{E_{m_2 - \vec{k},\beta} + E_{m_1 \vec{k},\alpha} - 2\,\mu}} \times \\
&\times \sqrt{\frac{f\left(-E_{n_2 - \vec{q},\beta} + \mu\right) - f\left(E_{n_1 \vec{q},\alpha} - \mu\right)}{E_{n_2 - \vec{q},\beta} + E_{n_1 \vec{q},\alpha} - 2\,\mu}}, \quad [9]
\end{aligned}$$

where $f(E)$ is the Fermi–Dirac distribution function. The detailed derivation of the Eqs. **8** and **9** is given in *SI Appendix*, section 4.

The condition for the onset of superconductivity is that the kernel Γ has an eigenvalue equal to 1. This defines the critical temperature, T_c, as the one at which the largest eigenvalue of Γ is equal to 1.

As the Hamiltonian of the TBG does not depend on the spin, we can identify two different kinds of vertices, depending on whether α and β share the same or opposite valley indices. These two vertices describe intravalley or intervalley superconductivity. As we argue in *SI Appendix*, section 4, the superconductivity is generally favored in the intervalley channel, and consequently we focus on that case in the following study.

Note, finally, that the potential $\mathcal{V}^{scr}_{\vec{G},\vec{G}'}(\vec{q})$ is repulsive. The attractive phonon-induced electron–electron interaction enters only in the screening function, and it is smaller than the Coulomb potential, except for Umklapp processes characterized by large reciprocal lattice vectors, $\vec{G}$. These terms are suppressed by the low electron polarizability at these wavevectors.

We neglect pairing due to the bare electron–phonon coupling. The dimensionless constant which describes approximately the phonon induced electron–electron interaction, $\overline{g} \approx 0.4$, implies weak-medium interaction, partially because only phonons of wavelength comparable to the moiré period can induce pairing.

A simple approximation which allows us to perform analytically the inversion of the dielectric matrix and to isolate diagonal and off diagonal Umklapp terms is given in *SI Appendix*, section 6.

Results

Results for the critical temperature for different angles and fillings are shown in Fig. 2*A*. The calculations take into account the Hartree potential, but not the exchange term. Note that, at the magic angle, $\theta = 1.085°$, and at half filling, when the Hartree potential vanishes, the system is metallic, with three pockets at the Fermi surface (see Fig. 2*B*). Note that the exchange potential, not considered here, leads to a gap at half filling (45–47). This gap is of order ∼20 to 40 meV, that is, much larger than the value of T_c calculated here. Hence, it seems likely that the insulating phase will prevail at half filling and close to a magic angle.

The value of T_c approximately follows the DOS at the Fermi level. As function of filling, the regions near van Hove singularities, which are displaced by the Hartree potential (40), give the maxima of T_c.

The results of Fig. 3 show that TBG is superconducting also in the absence of electron–phonon coupling. The critical temperature is of order $T_c \sim 10^{-2}$ K. Similar results, although with somewhat smaller values for the critical temperature, have been obtained in ref. 28.

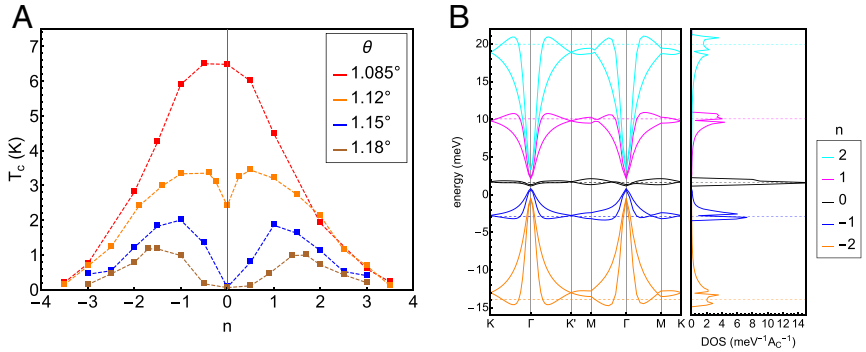

Fig. 2. (*A*) Values of the critical temperature as a function of filling for various angles (in our definition, $-4 \le n \le +4$, and $n = 0$ denotes the charge neutrality point). (*B*) Bands and DOS for the magical angle $\theta = 1.085°$ and different fillings. The horizontal lines mark the position of the Fermi energy.

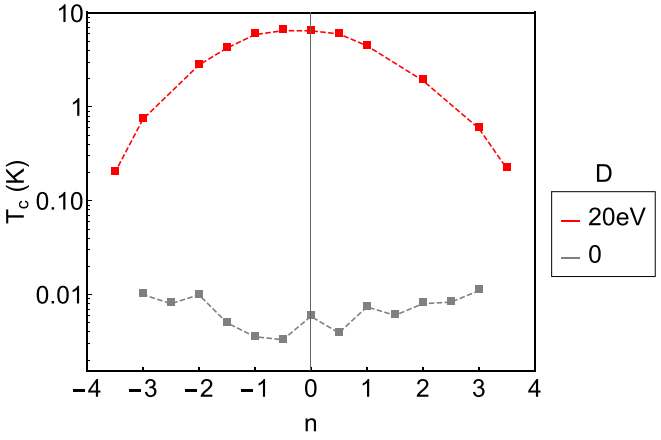

Fig. 3. Superconducting critical temperature with (red curve) and without (black curve) the electron–phonon contribution to the screening of the interaction. The calculation is at the magic angle, $\theta = 1.085°$. Note the logarithmic scale.

A discussion about the effect of the external screening on superconductivity is provided in *SI Appendix*, section 7. Remarkably, our results predict that superconductivity becomes more robust upon increasing the external screening, in good agreement with recent experimental findings (57).

In order to check if the superconductivity found here is related to the complexity of the wavefunctions of TBG (see, for instance, refs. 58–62), or it is a consequence of an enhanced DOS, we have performed calculations using the parameters in Fig. 2, including the electron–phonon coupling, neglecting the contribution from Umklapp processes. We obtain very low critical temperatures, of order $T_c \sim 10^{-4}$ K.

A comprehensive analysis of the role of Umklapp processes in the pairing is beyond the scope of this work. An estimate of their relevance can be inferred from the lowest order (zero and one bubble diagrams) in Fig. 1. Let us assume that the number of relevant reciprocal lattice vectors $\vec{G}$ is n_G (including $\vec{G} = 0$). For a momentum transferred $\vec{q}$, there are n_G direct interactions, defined by the bare interaction $v^C_{\vec{G}+\vec{q}}$. There are n_G^2 second-order diagrams, of order $v^C_{\vec{G}+\vec{q}} v^C_{\vec{G}'+\vec{q}} \chi_{\vec{G},\vec{G}'}(\vec{q})$. These diagrams are attractive, as $\chi_{\vec{G},\vec{G}'}(\vec{q}) < 0$. Hence, the combination of first- and second-order processes lead to an attractive interaction for $n_G \gg 1$ and $|\vec{q}| \sim |\vec{G}|$.

The relevance of Umklapp processes shows that, besides a large DOS, the nontrivial nature of the wave functions is crucial for the appearance of superconductivity.*

The absolute value and the phase of the order parameter projected onto the valence band throughout the BZ are shown in Fig. 4. For a filling $n = 0$ the width of the pair of bands is $\lesssim 1$ meV, and all the states in the central bands contribute to the pairing. The phase of the order parameter shows a change of sign, although lack of numerical accuracy prevents a precise determination of the symmetry, which seems close to p-wave. For $n = -2$, the order parameter is mostly localized in the vicinity of the two Fermi surfaces. The system resembles a two-gap superconductor, with generalized s-wave symmetry.

The number of pockets and detailed shape of the Fermi surface are highly dependent on the parameters of the model. A robust feature of our results, however, is the lack of sign changes of the order parameter along the Fermi surfaces, irrespective of their shape. A purely repulsive interaction favors sign changes, as in the p-wave pairing in ^{3}He or the d-wave pairing in the cuprates. We ascribe this effect to the fact that the screened interaction shows sizable attractive regions, as mentioned previously.

The calculations leading to the order parameter shown in Fig. 4 have been done assuming pairing between an electron in one valley with momentum $\vec{k}$ and another electron in the other valley, with momentum $-\vec{k}$ (see *SI Appendix*, section 4). Hence, the order parameter is compatible with spin singlet and spin triplet pairing, as the antisymmetry is ensured by using the right combination of the spin and valley components (66, 67).

Further results about the symmetry of the order parameter are reported in *SI Appendix*, section 8.

The approximate analysis of the pairing potential in *SI Appendix*, section 6 suggests that Umklapp processes favor pairing near the edges of the BZ and reduce it near its center, the Γ point. The role of Umklapp processes is further analyzed in *SI Appendix*, section 9.

Discussion

Main Results. The work presented here addresses two main topics:

- An analysis of the excitations of TBG. The calculations describe electron–hole pairs, plasmons, and acoustic phonons. For simplicity, we have only included longitudinal phonons, although the calculations can easily be extended to transverse acoustic (15) and to optical phonons (13). Intravalley phonons can be expected to increase further the superconducting pairing. The effect of intervalley optical phonons (13, 20) will enhance or suppress the pairing depending on whether the paired electrons are in a spin singlet/valley triplet or in a spin triplet/valley singlet combination.

The results reported here lead to the screening of the deformation potential and to the renormalization of both the electron–hole pairs and the phonon dispersion. The electron bands include the effects of the Hartree potential, but not exchange contributions.

We find a significant renormalization of the electron–hole continuum due to plasmons and phonons, and reciprocal changes in the phonon dispersion.

- We have analyzed superconducting pairing due to the repulsive Coulomb interaction screened by the excitations mentioned above. We do not consider here the direct, attractive, electron–phonon interaction, as it can be expected to give a small correction. Superconductivity is closely linked to the contribution of Umklapp processes.

Near half filling, where the central bands are narrowest, all states in the BZ contribute to the order parameter. Away from half filling, the weight of the order parameter is concentrated near the Fermi surface.

In most cases, we find that the order parameter has different weights in different pockets of the Fermi surface. The system resembles a multigap superconductor, with extended s-wave symmetry. The lack of sign changes in the order parameter, common in superconductivity derived from repulsive interactions, is due to the fact that Umklapp processes induce attractive terms in the superconducting kernel, Eq. **9** (see also *SI Appendix*, section 9). We have studied Cooper pairs made from electrons in different valleys. The resulting order parameter is compatible with spin singlet and with spin triplet pairing.

*The quantum metric associated to the wavefunctions in the Brillouin zone also affects the rigidity of the superconducting phase, and, as a result, it modifies the critical temperature (see refs. 63–65).

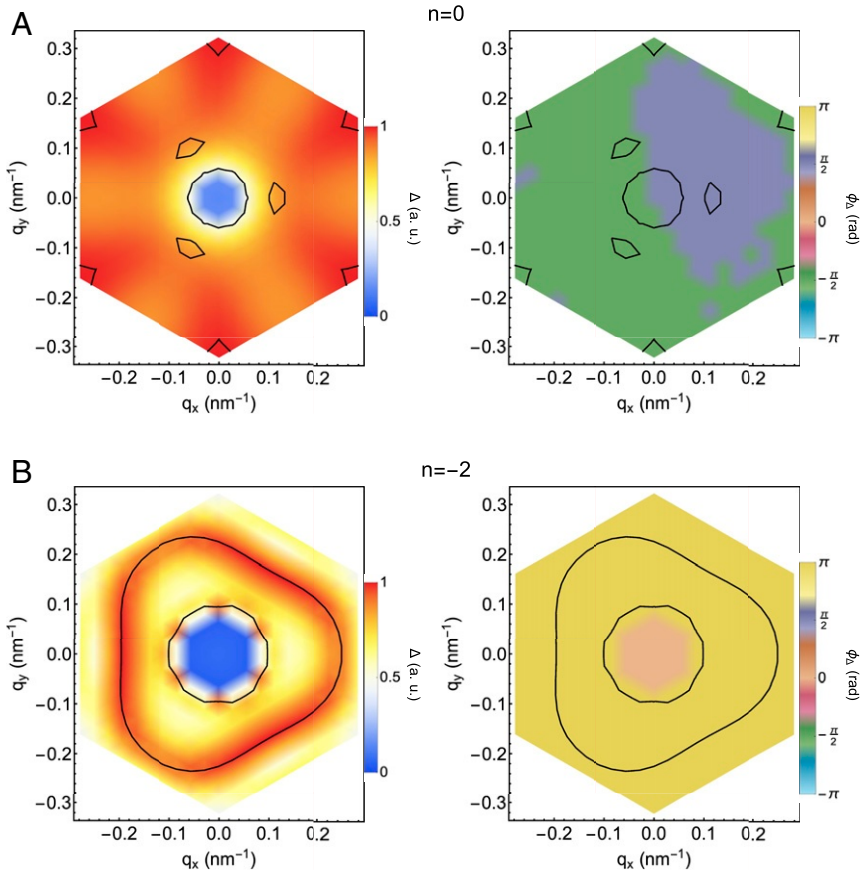

Fig. 4. Absolute value (*Left*) and phase (*Right*) of the order parameter projected onto the valence band throughout the BZ at the magic angle, $\theta = 1.085°$, and fillings $n = 0$ (*A*) and $n = -2$ (*B*). The black lines show the Fermi surface.

Other Effects. The work does not attempt to give numerically accurate predictions of the superconducting critical temperature, but the analysis is expected to give reasonable order of magnitude estimates, and to identify trends.

By considering together the role of electron–hole excitations, plasmons, and phonons in the dielectric function, we obtain values of T_c of the same order of magnitude as the experimentally measured ones. The value of T_c follows, approximately, the DOS at the Fermi surface. The suppression of the phonon contribution to the screening reduces the values of T_c by about two orders of magnitude. The neglect of the complexity of the wavefunctions, by leaving out Umklapp processes, reduces T_c by one or two orders of magnitude more, even including phonons. On the other hand, the order of magnitude of the critical temperature does not change when only the central bands are included in the calculation.

Our analysis does not consider exchange effects. In a fully symmmetric, metallic phase the exchange term is significantly smaller than the Hartree potential. The exchange contribution can lead to broken symmetry phases, where our analysis does not apply. Near a filling $n = \pm 2$, however, Hartree–Fock results (45) and the "cascade" picture of multiple phase transitions (51) lead to two completely full pairs of bands and two pairs of partially filled bands. If these bands belong to opposite valleys, our analysis, based on intervalley pairing, should be qualitatively correct.

For simplicity, we have not included the effect of transverse phonons, which couple to the electrons via a gauge potential (68, 69) (see also *SI Appendix*, section 3). The inclusion of these phonons will increase the tendency toward superconductivity. The frequency dependence of the phonon propagator, not considered here, leads to an upper bound in the value of T_c, which cannot exceed the phonon frequencies.

Elastic scattering is expected to induce pair breaking, as the order parameter has different values at different pockets. These effects will change substantially the superconducting properties when the elastic mean free path is comparable to the inverse of the separation between pockets, $\ell_{el} \sim |\Delta \vec{k}|^{-1}$. This estimate gives a mean free path a few times larger than the moiré wavelength. If the order parameter has opposite signs in the two valleys, defects which induce intervalley scattering will lead to subgap Andreev states.

Data Availability. All study data are included in the article and/or supporting information.

ACKNOWLEDGMENTS. We thank Leonid Levitov, Liang Fu, and José Maria Pizarro for many productive conversations. This work was supported by funding from the European Commission, under the Graphene Flagship, Core 3 Grant 881603 and by Grants NMAT2D (Comunidad de Madrid, Spain), SprQuMat, and SEV-2016-0686 (Ministerio de Ciencia e Innovación, Spain).

1. Y. Cao *et al.*, Correlated insulator behaviour at half-filling in magic-angle graphene superlattices. *Nature* **556**, 80–84 (2018).
2. Y. Cao *et al.*, Unconventional superconductivity in magic-angle graphene superlattices. *Nature* **556**, 43–50 (2018).
3. S. Doniach, The Kondo lattice and weak antiferromagnetism. *Physica B+C* **91**, 231–234 (1977).
4. G. R. Stewart, Heavy-fermion systems. *Rev. Mod. Phys.* **56**, 755–787 (1984).

5. G. R. Stewart, Superconductivity in iron compounds. *Rev. Mod. Phys.* **83**, 1589–1652 (2011).
6. B. Keimer, S. A. Kivelson, M. R. Norman, S. Uchida, J. Zaanen, From quantum matter to high-temperature superconductivity in copper oxides. *Nature* **518**, 179–186 (2015).
7. X. Lu *et al*., Superconductors, orbital magnets and correlated states in magic-angle bilayer graphene. *Nature* **574**, 653–657 (2019).
8. Y. Saito, J. Ge, K. Watanabe, T. Taniguchi, A. F. Young, Independent superconductors and correlated insulators in twisted bilayer graphene. *Nat. Phys.* **16**, 926–930 (2020).
9. H. S. Arora *et al*., Superconductivity in metallic twisted bilayer graphene stabilized by WSe_2. *Nature* **583**, 379–384 (2020).
10. P. Stepanov *et al*., Untying the insulating and superconducting orders in magic-angle graphene. *Nature* **583**, 375–378 (2020).
11. Y. Choi *et al*., Interaction-driven band flattening and correlated phases in twisted bilayer graphene. arXiv [Preprint] (2021). https://arxiv.org/abs/2102.02209 (Accessed 26 April 2021).
12. T. J. Peltonen, R. Ojajärvi, T. T. Heikkilä, Mean-field theory for superconductivity in twisted bilayer graphene. *Phys. Rev. B* **98**, 220504 (2018).
13. F. Wu, A. H. MacDonald, I. Martin, Theory of phonon-mediated superconductivity in twisted bilayer graphene. *Phys. Rev. Lett.* **121**, 257001 (2018).
14. Y. W. Choi, H. J. Choi, Strong electron-phonon coupling, electron-hole asymmetry, and nonadiabaticity in magic-angle twisted bilayer graphene. *Phys. Rev. B* **98**, 241412 (2018).
15. B. Lian, Z. Wang, B. A. Bernevig, Twisted bilayer graphene: A phonon-driven superconductor. *Phys. Rev. Lett.* **122**, 257002 (2019).
16. F. Wu, E. Hwang, S. Das Sarma, Phonon-induced giant linear-in-*t* resistivity in magic angle twisted bilayer graphene: Ordinary strangeness and exotic superconductivity. *Phys. Rev. B* **99**, 165112 (2019).
17. F. Schrodi, A. Aperis, P. M. Oppeneer, Prominent cooper pairing away from the Fermi level and its spectroscopic signature in twisted bilayer graphene. *Phys. Rev. Res.* **2**, 012066 (2020).
18. W. Qin, B. Zou, A. H. MacDonald, Critical magnetic fields and electron-pairing in magic-angle twisted bilayer graphene. arXiv [Preprint] (2021). https://arxiv.org/abs/2102.10504 (Accessed 26 April 2021).
19. Y. W. Choi, H. J. Choi, Dichotomy of electron-phonon coupling in graphene moire flat bands. arXiv [Preprint] (2021). https://arxiv.org/abs/2103.16132 (Accessed 26 April 2021).
20. M. Angeli, E. Tosatti, M. Fabrizio, Valley Jahn-Teller effect in twisted bilayer graphene. *Phys. Rev. X* **9**, 041010 (2019).
21. H. Isobe, N. F. Q. Yuan, L. Fu, Unconventional superconductivity and density waves in twisted bilayer graphene. *Phys. Rev. X* **8**, 041041 (2018).
22. Y. Sherkunov, J. J. Betouras, Electronic phases in twisted bilayer graphene at magic angles as a result of van hove singularities and interactions. *Phys. Rev. B* **98**, 205151 (2018).
23. J. González, T. Stauber, Kohn-luttinger superconductivity in twisted bilayer graphene. *Phys. Rev. Lett.* **122**, 026801 (2019).
24. D. V. Chichinadze, L. Classen, A. V. Chubukov, Nematic superconductivity in twisted bilayer graphene. *Phys. Rev. B* **101**, 224513 (2020).
25. Y. P. Lin, R. M. Nandkishore, Parquet renormalization group analysis of weak-coupling instabilities with multiple high-order Van Hove points inside the Brillouin zone. *Phys. Rev. B* **102**, 245122 (2020).
26. H. C. Po, L. Zou, A. Vishwanath, T. Senthil, Origin of mott insulating behavior and superconductivity in twisted bilayer graphene. *Phys. Rev. X* **8**, 031089 (2018).
27. Y.Z. You, A. Vishwanath, Superconductivity from valley fluctuations and approximate so(4) symmetry in a weak coupling theory of twisted bilayer graphene. *npj Quantum Materials* **4**, 1–12 (2019).
28. V. Kozii, M. P. Zaletel, N. Bultinck, Superconductivity in a doped valley coherent insulator in magic angle graphene: Goldstone-mediated pairing and Kohn-Luttinger mechanism. arXiv [Preprint] (2020). https://arxiv.org/abs/2005.12961 (Accessed 26 April 2021).
29. E. Khalaf, N. Bultinck, A. Vishwanath, M. P. Zaletel, Soft modes in magic angle twisted bilayer graphene. arXiv [Preprint] (2020). https://arxiv.org/abs/2009.14827 (Accessed 26 April 2021).
30. A. Kumar, M. Xie, A. H. MacDonald, Lattice collective modes from a continuum model of magic-angle twisted bilayer graphene. arXiv [Preprint] (2020). https://arxiv.org/abs/2010.05946 (Accessed 26 April 2021).
31. F. Wu, S. Das Sarma, Collective excitations of quantum anomalous hall ferromagnets in twisted bilayer graphene. *Phys. Rev. Lett.* **124**, 046403 (2020).
32. B. Roy, V. Juričić, Unconventional superconductivity in nearly flat bands in twisted bilayer graphene. *Phys. Rev. B* **99**, 121407 (2019).
33. Z. A. H. Goodwin, F. Corsetti, A. A. Mostofi, J. Lischner, Attractive electron-electron interactions from internal screening in magic-angle twisted bilayer graphene. *Phys. Rev. B* **100**, 235424 (2019).
34. C. Lewandowski, D. Chowdhury, J. Ruhman, Pairing in magic-angle twisted bilayer graphene: Role of phonon and plasmon Umklapp. arXiv [Preprint] (2020). https://arxiv.org/abs/2007.15002 (Accessed 26 April 2021).
35. G. Sharma, M. Trushin, O. P. Sushkov, G. Vignale, S. Adam, Superconductivity from collective excitations in magic-angle twisted bilayer graphene. *Phys. Rev. Res.* **2**, 022040 (2020).
36. W. Kohn, J. M. Luttinger, New mechanism for superconductivity. *Phys. Rev. Lett.* **15**, 524–526 (1965).
37. J. M. Pizarro, M. Rösner, R. Thomale, R. Valentí, T. O. Wehling, Internal screening and dielectric engineering in magic-angle twisted bilayer graphene. *Phys. Rev. B* **100**, 161102 (2019).
38. C. Lewandowski, L. Levitov, Intrinsically undamped plasmon modes in narrow electron bands. *Proc. Natl. Acad. Sci. U.S.A.* **116**, 20869–20874 (2019).
39. F. Guinea, N. R. Walet, Electrostatic effects, band distortions, and superconductivity in twisted graphene bilayers. *Proc. Natl. Acad. Sci. U.S.A.* **115**, 13174–13179 (2018).
40. T. Cea, N. R. Walet, F. Guinea, Electronic band structure and pinning of Fermi energy to Van Hove singularities in twisted bilayer graphene: A self-consistent approach. *Phys. Rev. B* **100**, 205113 (2019).
41. L. Rademaker, D. A. Abanin, P. Mellado, Charge smoothening and band flattening due to Hartree corrections in twisted bilayer graphene. *Phys. Rev. B* **100**, 205114 (2019).
42. M. J. Calderón, E. Bascones, Interactions in the 8-orbital model for twisted bilayer graphene. *Phys. Rev. B* **102**, 155149 (2020).
43. Z. A. H. Goodwin, V. Vitale, X. Liang, A. A. Mostofi, J. Lischner, Hartree theory calculations of quasiparticle properties in twisted bilayer graphene. *Electronic Structure* **2**, 034001 (2020).
44. M. Xie, A. H. MacDonald, Nature of the correlated insulator states in twisted bilayer graphene. *Phys. Rev. Lett.* **124**, 097601 (2020).
45. T. Cea, F. Guinea, Band structure and insulating states driven by Coulomb interaction in twisted bilayer graphene. *Phys. Rev. B* **102**, 045107 (2020).
46. Y. Zhang, K. Jiang, Z. Wang, F. Zhang, Correlated insulating phases of twisted bilayer graphene at commensurate filling fractions: A Hartree-Fock study. *Phys. Rev. B* **102**, 035136 (2020).
47. S. Liu, E. Khalaf, J. Y. Lee, A. Vishwanath, Nematic topological semimetal and insulator in magic-angle bilayer graphene at charge neutrality. *Phys. Rev. Res.* **3**, 013033 (2021).
48. C. C. Liu, L. D. Zhang, W. Q. Chen, F. Yang, Chiral spin density wave and d+id superconductivity in the magic-angle-twisted bilayer graphene. *Phys. Rev. Lett.* **121**, 217001 (2018).
49. N. Bultinck *et al*., Ground state and hidden symmetry of magic-angle graphene at even integer filling. *Phys. Rev. X* **10**, 031034 (2020).
50. J. Liu, X. Dai, Theories for the correlated insulating states and quantum anomalous hall effect phenomena in twisted bilayer graphene. *Phys. Rev. B* **103**, 035427 (2021).
51. U. Zondiner *et al*., Cascade of phase transitions and Dirac revivals in magic-angle graphene. *Nature* **582**, 203–208 (2020).
52. J. M. B. Lopes Dos Santos, N. M. R. Peres, A. H. Castro Neto, Graphene bilayer with a twist: Electronic structure. *Phys. Rev. Lett.* **99**, 256802 (2007).
53. R. Bistritzer, A. H. MacDonald, Moire bands in twisted double-layer graphene. *Proc. Natl. Acad. Sci. U.S.A.* **108**, 12233–12237 (2011).
54. M. Koshino *et al*., Maximally localized wannier orbitals and the extended Hubbard model for twisted bilayer graphene. *Phys. Rev. X* **8**, 031087 (2018).
55. F. Guinea, N. R. Walet, Continuum models for twisted bilayer graphene: Effect of lattice deformation and hopping parameters. *Phys. Rev. B* **99**, 205134 (2019).
56. C. Lewandowski, S. Nadj-Perge, D. Chowdhury, Does filling-dependent band renormalization aid pairing in twisted bilayer graphene? arXiv [Preprint] (2021). https://arxiv.org/abs/2102.05661 (Accessed 26 April 2021).
57. X. Liu *et al*., Tuning electron correlation in magic-angle twisted bilayer graphene using Coulomb screening. *Science* **371**, 1261–1265 (2021).
58. H. C. Po, H. Watanabe, A. Vishwanath, Fragile topology and Wannier obstructions. *Phys. Rev. Lett.* **121**, 126402 (2018).
59. H. C. Po, L. Zou, T. Senthil, A. Vishwanath, Faithful tight-binding models and fragile topology of magic-angle bilayer graphene. *Phys. Rev. B* **99**, 195455 (2019).
60. Z. Song *et al*., All magic angles in twisted bilayer graphene are topological. *Phys. Rev. Lett.* **123**, 036401 (2019).
61. K. Hejazi, C. Liu, H. Shapourian, X. Chen, L. Balents, Multiple topological transitions in twisted bilayer graphene near the first magic angle. *Phys. Rev. B* **99**, 035111 (2019).
62. V. T. Phong, E. J. Mele, Obstruction and interference in low-energy models for twisted bilayer graphene. *Phys. Rev. Lett.* **125**, 176404 (2020).
63. X. Hu, T. Hyart, D. I. Pikulin, E. Rossi, Geometric and conventional contribution to the superfluid weight in twisted bilayer graphene. *Phys. Rev. Lett.* **123**, 237002 (2019).
64. A. Julku, T. J. Peltonen, L. Liang, T. T. Heikkilä, P. Törmä, Superfluid weight and Berezinskii-Kosterlitz-Thouless transition temperature of twisted bilayer graphene. *Phys. Rev. B* **101**, 060505 (2020).
65. F. Xie, Z. Song, B. Lian, B. A. Bernevig, Topology-bounded superfluid weight in twisted bilayer graphene. *Phys. Rev. Lett.* **124**, 167002 (2020).
66. M. S. Scheurer, R. Samajdar, Pairing in graphene-based moiré superlattices. *Phys. Rev. Res.* **2**, 033062 (2020).
67. E. Khalaf, P. Ledwith, A. Vishwanath, Symmetry constraints on superconductivity in twisted bilayer graphene: Fractional vortices, 4e condensates or non-unitary pairing. arXiv [Preprint] (2020). https://arxiv.org/abs/2012.05915 (Accessed 26 April 2021).
68. A. H. Castro Neto, F. Guinea, N. M. R. Peres, K. S. Novoselov, A. K. Geim, The electronic properties of graphene. *Rev. Mod. Phys.* **81**, 109–162 (2009).
69. M. Vozmediano, M. Katsnelson, F. Guinea, Gauge fields in graphene. *Phys. Rep.* **496**, 109–148 (2010).